Electronic structure and phonon properties in the kagome metals RT_3B_2 (R = Y, Lu; T = Co, Os)

Savita Chaudhary,[1] Armando Consiglio,[2,3] Jaskaran Singh,[4] Domenico Di Sante,[3,5] Ronny Thomale,[2] and Yogesh Singh[1]

[1]*Department of Physical Sciences, Indian Institute of Science Education and Research (IISER) Mohali, Knowledge City, Sector 81, Mohali 140306, India*

[2]*Institut für Theoretische Physik und Astrophysik and Würzburg-Dresden Cluster of Excellence ct.qmat, Universität Würzburg, 97074 Würzburg, Germany*

[3]*CNR - Istituto Officina dei Materiali (IOM), S.S. 14 km 163.5, 34149 Trieste, Italy*

[4]*Department of Physics, Punjabi University, Patiala 147002, India*

[5]*Department of Physics and Astronomy, Alma Mater Studiorum, University of Bologna, 40127 Bologna, Italy*

(Received 5 July 2025; revised 29 November 2025; accepted 9 December 2025; published 29 December 2025)

The RT_3B_2 (R = Y, Lu, T = Co, Os) family hosts a perfect kagome lattice of T atoms, offering an interesting platform to investigate the interplay of electronic structure, superconductivity, and lattice dynamics. Here, we compare two members of this family, $LuOs_3B_2$ and YCo_3B_2, with similar crystallography but differing chemical composition, which results in different electronic structures and correlation signatures, as well as distinct spin-orbit coupling effects. We confirm superconductivity in $LuOs_3B_2$ with $T_c = 4.75$ K, while YCo_3B_2 remains nonsuperconducting above 1.8 K. Both materials exhibit kagome-derived electronic features, including quasiflat bands, Dirac cones, and van Hove singularities. Fermi surface calculations reveal a highly anisotropic electronic structure in YCo_3B_2, establishing a k_z-selective metallic behavior and leading to strongly suppressed in-plane conduction, in contrast to the more isotropic fermiology of $LuOs_3B_2$. Phonon calculations for $LuOs_3B_2$ show imaginary modes, indicating potential lattice instabilities. Experimental estimates of the Wilson and Kadowaki-Woods ratios point to significant electronic correlations in both compounds.

DOI: 10.1103/cdjy-6jgs

I. INTRODUCTION

The kagome lattice has attracted a lot of attention recently due to its ability to host novel physics because of its distinctive electronic structure [1–4]. Insulating materials with a kagome lattice host localized magnetic moments, serving as ideal systems to investigate geometrically frustrated magnetism. A prominent example is the quantum spin liquid (QSL) state observed in herbertsmithite where the kagome layers of copper ions exhibit long-range quantum entanglement and fractionalized spinon excitations without conventional magnetic order [5,6]. Beyond two dimensions, insulating quantum magnets with three-dimensional kagome-inspired lattices have also demonstrated novel frustration-driven phenomena and QSL behavior [7–9]. Recent attention has shifted to metallic kagome systems, where the interplay of topology and electron correlations becomes possible. Theoretical predictions highlight the coexistence of Dirac cones, flat bands, and van Hove singularities in the electronic band structure [10], creating opportunities for exotic electronic states. Experimental advances have identified several families of metallic kagome materials, such as the predicted herbertsmithite related material $GaCu_3(OH)_6Cl_2$ [10], FeSn and CoSn compounds [11,12], and the 166 compounds, e.g., YMn_6Sn_6 [13], which realize these electronic features. Recently, the AV_3Sb_5 (A = K, Rb, Cs) family of materials has been discovered, featuring an ideal kagome lattice formed by vanadium ions. These compounds display signatures of strong electronic correlations and nontrivial topological characteristics, leading to novel behaviors like the emergence of charge density waves, superconductivity, and the anomalous Hall effect [14–17].

RT_3X_2 (R = lanthanide, $T = 3d$, $4d$, or $5d$ transition metal, X = Si, B) is another family of materials hosting the kagome lattice which was discovered in the 1980s and 1990s [18–20], and several of its members were found to be superconducting with T_c between 1 and ≈7 K [18–23]. The majority of these investigations, however, did not make a connection of the physical properties with the underlying kagome lattice. Recently, several unconventional properties were reported in $LaRu_3Si_2$, the material having the highest $T_c = 7$ K in this family, $ThRu_3Si_2$ and YRu_3Si_2, possibly arising from electron correlations from the flat bands [24–28]. We recently reported on $LaRh_3B_2$, which contains the essential fermiology of the two-dimensional (2D) kagome lattice. The material shows superconductivity at $T_c \sim 2.6$ K but did not show any experimental evidence of the charge density wave (CDW) state. Lack of significant electronic correlations in $LaRh_3B_2$ suggests that electronic correlations might play an important role in the existence of CDW states observed in other kagome metals [29]. The RT_3X_2 family, which can be synthesized for $T = 3d$, $4d$, or $5d$ transition metals, offers the opportunity to vary the strength of electronic correlations and spin-orbit coupling (SOC) through changes in chemical composition.

In this work, we synthesize and study YCo_3B_2 and $LuOs_3B_2$ through measurements of their electronic transport, magnetic susceptibility, and heat capacity and through calculations of their electronic structure, Fermi surfaces (Fig. 4),

and phonon spectrum. This choice of materials enables an analysis of how structural and chemical differences influence correlation signatures and spin-orbit coupling within the RT_3B_2 kagome family. Our measurements show that YCo_3B_2, and to a greater extent $LuOs_3B_2$, host strong electronic correlation, as evidenced by the enhanced values of the Wilson and the Kadowaki-Woods ratios. Additionally, the $LuOs_3B_2$ phonon spectra show imaginary modes pointing to a susceptibility to lattice instabilities. Our work therefore provides a connection between electron correlation and structural or CDW-like tendencies in RT_3B_2 kagome metals.

II. METHODS

Polycrystalline samples of YCo_3B_2 and $LuOs_3B_2$ were synthesized by arc-melting stoichiometric amounts of high purity elements. The melted buttons were flipped over and melted five to ten times to promote homogeneity. Powder x-ray diffraction (PXRD) on a Bruker D8 Advance diffractometer system with Cu-Kα radiation was used to determine the phase purity of the synthesized materials. The relative stoichiometry of R and T was confirmed using energy dispersive spectroscopy using a scanning electron microscope. The dc magnetic susceptibility χ, heat capacity C, and electrical transport were measured using a Quantum Design Physical Property Measurement System equipped with a He3 insert.

To theoretically simulate the electronic structure of RT_3B_2, we performed first-principles density functional theory (DFT) calculations. The electronic structure calculations were carried out using VASP [30–33], while the phonon spectra were obtained with QUANTUM ESPRESSO [34–36]. Concerning vasp, we considered the projector-augmented wave (PAW) pseudopotential with the exchange-correlation functional of the generalized gradient approximation (GGA) of Perdew-Burke-Ernzerhof [37,38]. We adopted a $9 \times 9 \times 12$ k-mesh for the first Brillouin zone and an energy cutoff of 550 eV for the plane-wave basis. The convergence criteria for energy is set to 10^{-6} eV. When considered, SOC was included self-consistently. Phonon calculations were performed using density functional perturbation theory, as implemented in QUANTUM ESPRESSO [34–36]. Exchange and correlation effects were included using the generalized GGA with the Perdew-Burke-Ernzerhof (PBE) functional [38]; the pseudopotentials are norm-conserving, with core correction, and scalar relativistic [39]. In particular, we employed scalar-relativistic pseudopotentials generated with the oncvpsp code (version 3.3.0, 08/16/2017, D. R. Hamann)

Self-consistent calculations of the previously relaxed unit cell were performed with a $6 \times 6 \times 12$ k-grid. The kinetic energy cutoff for the wave functions is equal to 100 Ry, while the cutoff for charge density is 400 Ry. The convergence threshold for ionic minimization and electronic self-consistency are set to be 1.0D-15 Ry/Bohr and 1.0D-15 Ry, respectively. The self-consistency threshold for phonon calculations is 1.0D-15 Ry as well, with a q-grid of $3 \times 3 \times 6$ for YCo_3B_2 and $6 \times 6 \times 6$ for $LuOs_3B_2$. Non-self-consistent calculations for the density of states were performed with a $30 \times 30 \times 30$ grid. Finally, the electron-phonon interaction is computed via an interpolation over the Brillouin zone [40].

III. STRUCTURE

Both samples, $LuOs_3B_2$ and YCo_3B_2, crystallize in a honeycomb structure with space group $P6/mmm$. With the exception of the unit cell size, the structure has no variable parameters. A Rietveld refinement of the powder patterns on the basis of hexagonal $P6/mmm$ symmetry as shown in Figs. 1(a) and 1(b) five the lattice parameters $a = 5.456$ Å, $c = 3.064$ Å, $a = 5.033$ Å, and $c = 3.037$ Å for $LuOs_3B_2$ and YCo_3B_2, respectively. These lattice parameters are in good agreement with prior reports [18,41]. From the powder XRD data we find that there are two additional phases, i.e., $\approx$2% $LuOsB_4$ and $\approx$3% Os in the case of $LuOs_3B_2$. These impurity phases do not allow a good Rietveld refinement. Therefore, only lattice parameters from the positions of the Bragg peaks will be quoted and no other refinement parameters are used in our study. Repeated attempts with varying starting stoichiometry to produce single-phase samples were unsuccessful. This indicates that $LuOs_3B_2$ is most likely incongruently melting in nature and cannott be produced as a single phase from the melt. We also observe a tiny amount of Y ($\approx$1%) in the XRD data for YCo_3B_2.

Figure 1(d) shows the schematic of the crystal structure of the samples, where the central atoms Os and Co are arranged in perfect kagome layers. These kagome layers of Os(Co) are separated by layers of Lu(Y) and B stacked along the c-axis as shown in Fig. 1(c). Thus, the description of the crystal structure hints that these substances possess the structural components necessary to exhibit the electronic structure characteristics anticipated of a kagome metal. It must be noted, however, that the short c-axis could imply that coupling between kagome planes may be significant.

IV. RESULTS

A. Electronic structure

Figure 2 shows the electronic band structure with and without SOC for $LuOs_3B_2$ and YCo_3B_2 along some high-symmetry directions in the Brillouin zone. The metallic nature of both materials is evident as several bands can be seen crossing the Fermi level. A comparison of the two compounds suggests that electronic correlations are expected to be more relevant in YCo_3B_2. In particular, the bands of YCo_3B_2 are narrower and less dispersive than those of $LuOs_3B_2$, which qualitatively points to enhanced correlation effects in the Co-based compound. This expectation is also consistent with the different orbital character: Co $3d$ states are generally more localized than Os $5d$ states, and therefore more prone to correlation effects. Whereas the inclusion of SOC has the most significant effect in the band structure of $LuOs_3B_2$ and is almost negligible for YCo_3B_2. We also note the high density of states in YCo_3B_2 at energies between 0.5 and 1 eV below the Fermi energy E_F. It could be of interest to enhance the density of states at E_F by shifting the valence bands upward via strain/pressure or doping.

We now turn to the features of the band structure expected to arise from the kagome lattice. The band structure of both materials show a quasiflat band (FB) in the Γ-M-K-Γ direction. YCo_3B_2 shows additional flat-band features in the Γ - A direction. Dirac cones (DC) are observed at the K point of the Brillouin zone. The DCs are closer to E_F for $LuOs_3B_2$. We

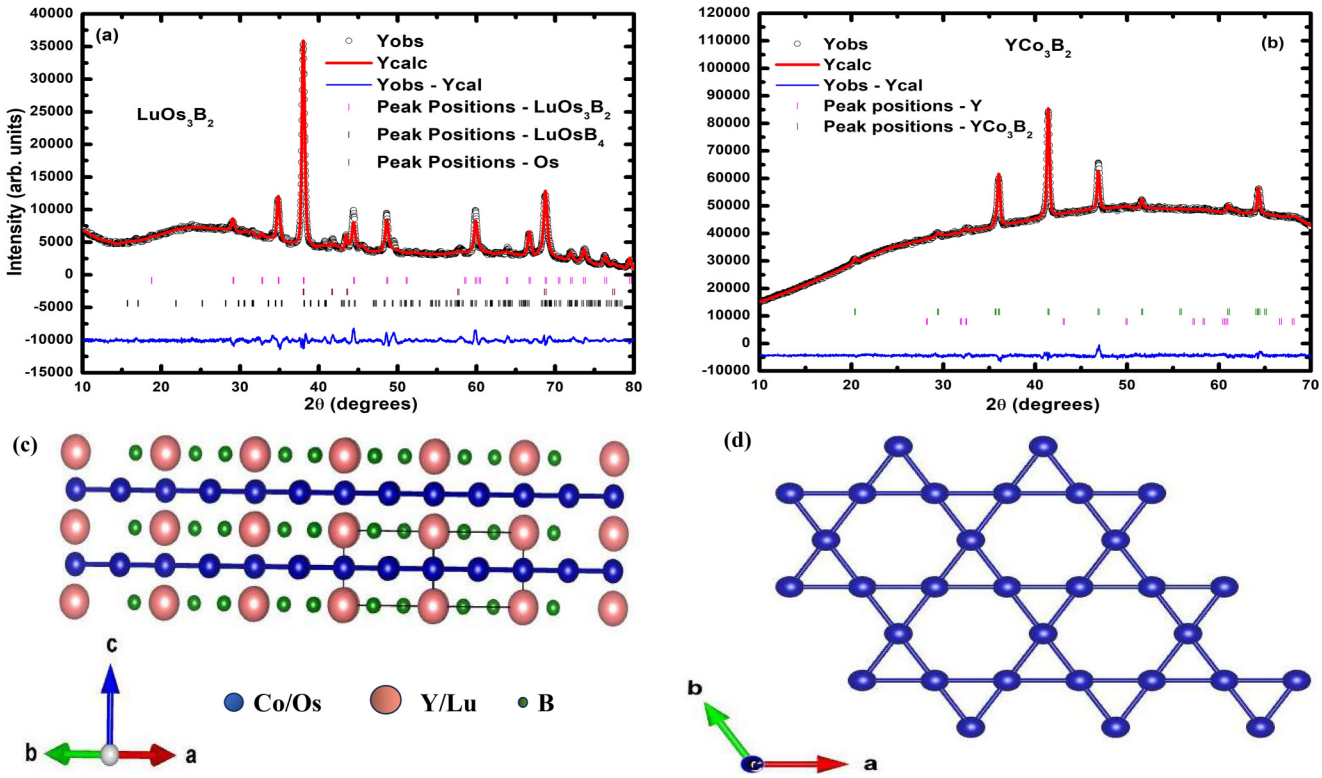

FIG. 1. Powder x-ray diffraction and results of refinement for (a) $LuOs_3B_2$ and (b) YCo_3B_2. A schematic of the crystal structure of RT_3B_2 viewed (c) perpendicular to the crystallographic c-axis showing the layered nature of the structure with T atomic planes separated along the c-axis by planes made up of R and B atoms. (d) Viewed along the c-axis, the T atoms form an undistorted kagome lattice.

also identify van Hove singularities (VHS) located at the M points for both materials.

The kagome lattice related features in the band structure arise primarily from the Co and Os orbitals as shown in the element specific band structures shown in Fig. 3. It is also evident that bands close to E_F mostly arise from the kagome network. Figure 3 shows the orbital contributions from Co and Os to the band structure for both materials. We note that for YCo_3B_2 there are no states at E_F for $k_z = 0.0$. Most of the states at E_F come from d_{xz} and d_{yz} orbitals, at $k_z = 0.5$. For $LuOs_3B_2$, d_{xz} and d_{yz} orbitals contribute more for $k_z = 0.0$ while $d_{x^2-y^2}$ and d_{xy} contribute more for $k_z = 0.5$.

We recall that we previously reported similar kagome band-structure features for $LaRh_3B_2$ [29] indicating that the RT_3B_2 family of kagome metals possesses the predicted features of the 2D kagome lattice band structure near E_F with additional modifications arising most likely from the three-dimensional nature of the material.

The Fermi surface of YCo_3B_2, shown in Fig. 4(c), displays a k_z-selective metallic character. At $k_z = 0$ the system is fully gapped and no states cross the Fermi level. Small Fermi-surface pockets appear only for $|k_z| \geqslant 0.3$, indicating that the in-plane electronic structure is effectively insulating, while conduction occurs only along the stacking direction

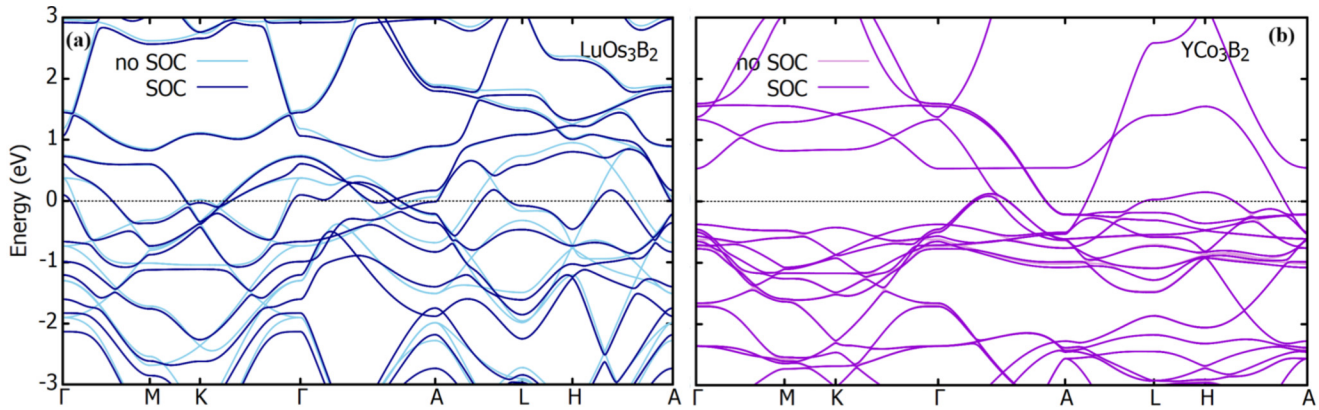

FIG. 2. Electronic structure along high-symmetry paths in k-space, compared with and without SOC cases, for (a) $LuOs_3B_2$ and (b) YCo_3B_2. In both panels, the Fermi level is located at 0 eV.

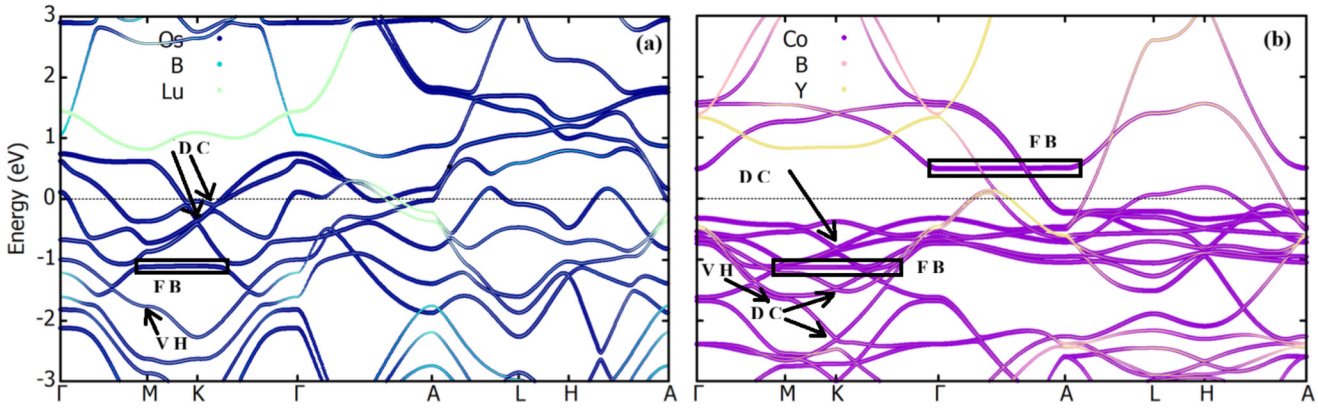

FIG. 3. Elemental contributions to the electronic band structure of (a) $LuOs_3B_2$ and (b) YCo_3B_2. In both panels, the Fermi level is located at 0 eV.

within narrow k_z intervals. This highly anisotropic electronic topology underscores the layered and direction-dependent transport properties of YCo_3B_2.

B. Physical properties

We now discuss the electrical, magnetic, and thermal properties of $LuOs_3B_2$ in the normal and superconducting states. Figure 5(a) shows the electrical resistivity of $LuOs_3B_2$ measured in the temperature range of 2 to 375 K at zero field, which confirms the metallic behavior of $LuOs_3B_2$ with a residual resistivity ratio RRR $= \rho(375\ \mathrm{K})/\rho(5\ \mathrm{K}) \approx 11$. The $\rho(T)$ in the low-temperature region was fit by the equation $\rho(T) = \rho_0(T) + aT^2 + bT^5$, where $\rho_0(T)$ is the residual resistivity and the terms aT^2 and bT^5 arise from electron-electron and electron-phonon scattering, respectively. Fitting the $\rho(T)$ data in the temperature range (5 K $< T <$ 35 K) gives the fit parameters $\rho_0 = 9.68\ \mu\Omega$ cm, $a = 9.7\times10^{-3}\ \mu\Omega$ cm K^{-2}, and $b = 3.03 \times 10^{-8}\ \mu\Omega$ cm K^{-5}. A considerably small value of b as compared to a for $T < 35$ K suggests that the resistivity in the low-temperature region is mainly governed by electron-electron scattering. The inset shows the resistivity data from $T = 4$ to 5.5 K at various applied fields to highlight the onset of superconductivity in $LuOs_3B_2$ indicated by the sharp drop to zero resistance below $T_c \approx 4.9$ K in the zero field. This is consistent with T_c values reported previously [18,21]. The suppression of the superconducting transition to a lower temperature on increasing magnetic field is evident in the resistivity data shown in the inset of Fig. 5(a). Figure 5(b) shows the magnetic susceptibility χ versus temperature T plotted between 2 and 305 K in an applied magnetic field of $H = 2$ T. For a Pauli paramagnetic metal, a T-independent magnetic susceptibility is expected, described by $\chi_p = \mu_B^2 D(\varepsilon_F)$, where μ_B is the Bohr magneton and $D(\varepsilon_F)$ is the electronic density of states at the Fermi level. However, in $LuOs_3B_2$, the susceptibility is found to be temperature-dependent across the entire measured temperature range. This observation is similar to $LaRh_3B_2$ which we reported previously [29]. The Curie-like upturn at low temperatures in $\chi(T)$ is expected to arise from trace amounts of magnetic impurities in the starting elements used to synthesize the materials. We have therefore fitted the $\chi(T)$ in the full temperature range with the expression $\chi(T) = \chi_0[1 - (T/T_E)^2] + C/(T - \theta)$, where the first term represents the T-dependent Pauli paramagnetic susceptibility, the second term accounts for contributions from trace amounts of magnetic impurities.

The fitting parameters are the temperature-independent average Pauli paramagnetic susceptibility, χ_0; a phenomenological

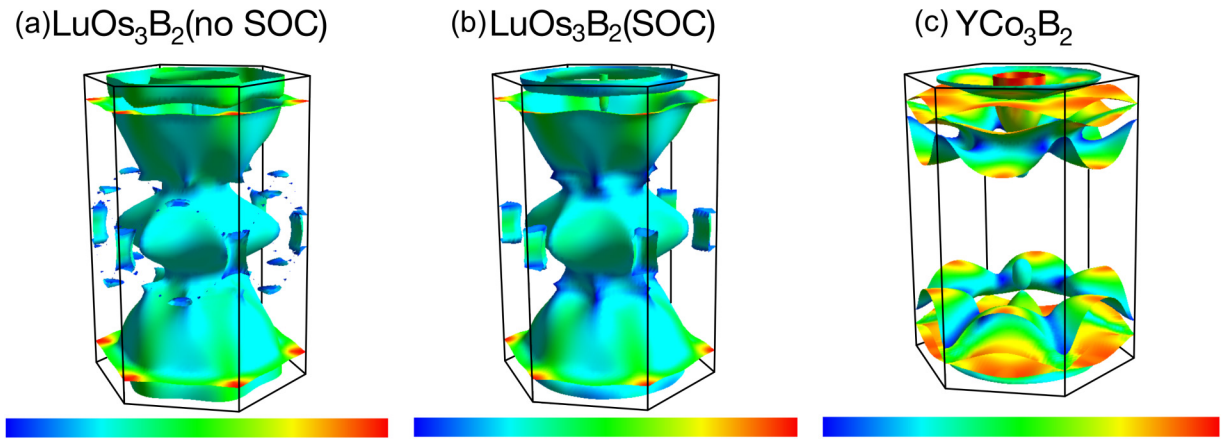

FIG. 4. (a), (b) Showing Fermi surface of $LuOs_3B_2$ with and without SOC, respectively, and (c) of YCo_3B_2. The color scale indicates the Fermi velocity.

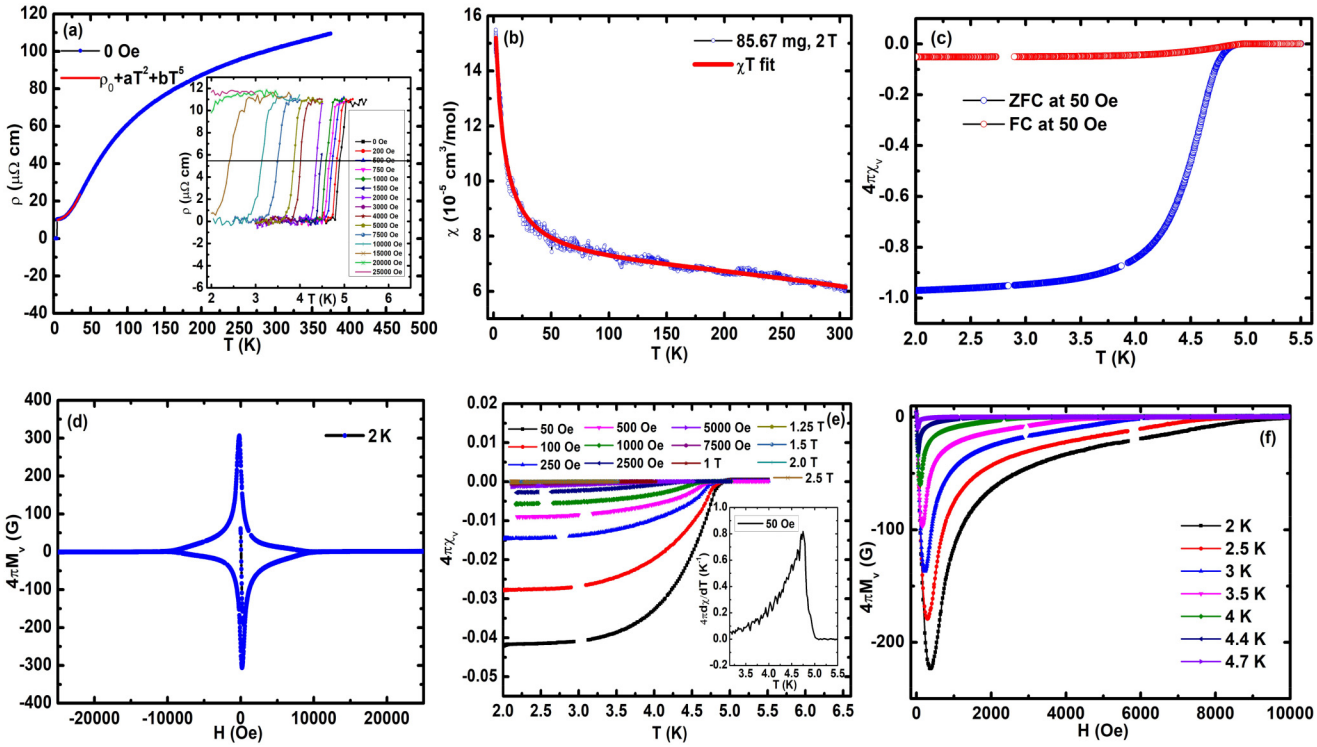

FIG. 5. Panel (a) shows the electrical resistivity of $LuOs_3B_2$ measured in the temperature range of 2.5 to 375 K at zero field, the inset shows the resistivity data between 4 to 5.5 K at various applied fields. Panel (b) shows the magnetic susceptibility χ versus temperature T curve plotted between 2 and 305 K in an applied magnetic field of $H = 2$ T. Panel (c) shows the temperature dependence of the dimensionless magnetic susceptibility $4\pi\chi$ in the zero-field-cooled warming and the field-cooled cooling mode measured at 50 Oe. Panel (d) shows the hysteresis loop at 2 K of the volume magnetization M_v(H) normalized by $1/4\pi$, versus applied magnetic field H. Panel (e) shows the temperature dependence of the field-cooled dimensionless magnetic susceptibility ($4\pi\chi$) at various fields and the inset shows the derivative of $4\pi\chi$ w.r.t T. Panel (f) shows the volume magnetization $M_v(H)$ normalized by $1/4\pi$ versus applied magnetic field H at various temperatures.

parameter related to the Fermi energy, T_E; the Curie constant of the impurities, C; and the Weiss temperature θ, representing any interactions between the magnetic impurities. The fitting curve shown as the solid curve through the data in Fig. 5(b) estimates $\chi_0 = 6.74(1) \times 10^{-5}$ cm^3/mol, $T_E = 884(7)$ K, $C = 0.00068(1)$ cm^3 K/mol, and $\theta = -6.1(1)$ K. The obtained value of C is equivalent to 0.17% of $S = 1/2$ impurities, which is quite small.

The temperature-independent susceptibility can be expressed as $\chi_0 = \chi_{\text{core}} + \chi_P + \chi_{VV} + \chi_L$ where χ_{core} is the diamagnetic orbital contribution from the electrons (ionic or atomic), χ_P is the Pauli paramagnetic susceptibility of conduction electrons, χ_{VV} is the Van Vleck paramagnetic orbital contribution, and χ_L is the Landau orbital diamagnetism of conduction electrons ($\chi_L \approx \frac{-1}{3}\chi_P$). Assuming the covalent nature of the bonds in $LuOs_3B_2$, we take the atomic diamagnetism values χ_{core} [42] for Lu (-60.55×10^{-6} cm^3/mol), Os (-53.82×10^{-6} cm^3/mol), and B (-12.54×10^{-6} cm^3/mol) from which we get $\chi_{\text{core}} = -2.47 \times 10^{-4}$cm^3/mol. The Van Vleck paramagnetic orbital contribution is neglected giving $\chi_P = 5.72 \times 10^{-4}$ cm^3/mol.

We now present an observation of superconductivity. Figure 5(c) shows the temperature dependence of the dimensionless magnetic susceptibility $4\pi\chi$ in the zero-field-cooled (ZFC) warming and the field-cooled (FC) cooling mode measured in a magnetic field of 50 Oe. The presence of a diamagnetic signal in the ZFC and the FC data below $T_c \approx$ 4.75 K confirms the superconducting transition in $LuOs_3B_2$. The field-cooled data have a weak diamagnetic signal which points towards strong pinning in the sample suggesting type-II superconductivity in $LuOs_3B_2$ which we confirm below using magnetization measurements. Figure 5(d) shows the hysteresis loop at 2 K of the volume magnetization M_v(H) normalized by $1/4\pi$, versus the applied magnetic field H. The hysteresis loop is typical of a type-II superconductor. Figures 5(e) and 5(f) show the temperature dependence of $4\pi\chi$ at various fields and $4\pi M_v(H)$ at various temperatures, respectively. We will use these data to extract the upper critical field as a function of temperature.

The heat capacity measurements provide evidence for the bulk nature of superconductivity in $LuOs_3B_2$. Figure 6(a) shows the heat capacity C measured between 2 and 10 K at 0 Oe as well as at 5 T. The anomaly with an onset at $\approx$4.9 K signals a transition into the superconducting state. The $C(T)$ data in 5 T then provides the normal state heat capacity. The heat capacity in the normal state can be expressed as $C = \gamma_n T + \beta T^3$ where γ_n is the normal-state Sommerfeld coefficient and the second term accounts for the lattice contribution. A fit of the normal-state heat capacity data to the above expression gives the fitting parameters $\gamma_n = 14.28(9)$ mJ/mol K^2 and $\beta = 0.261(6)$ mJ/mol K^4. Using this value of β, we calculate a Debye temperature of $\theta_D = 355(3)$ K [43]. The electronic heat capacity can then be extracted from the total heat capacity by subtracting the lattice

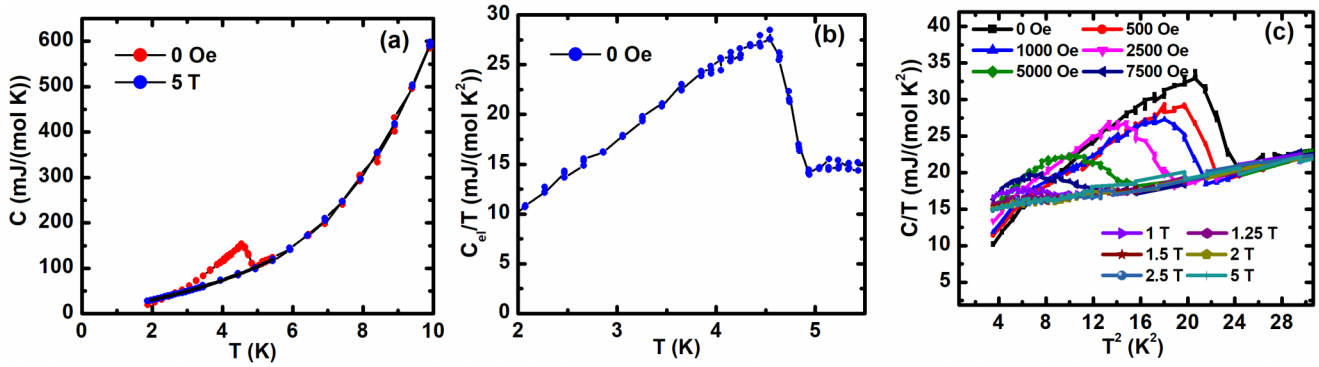

FIG. 6. (a) Heat capacity between 2 to 10 K at 0 Oe as well as at 5 T, (b) the electronic heat capacity $C_{\rm el}$ divided by T versus T and (c) C/T versus T^2 at various magnetic fields.

contribution. Figure 6(b) shows the resultant electronic heat capacity $C_{\rm el}$ divided by T versus T, which reveals a transition from the normal to the superconducting state with critical temperature $T_c \approx 4.75$ K. The initial analysis of the heat capacity data measures down to 2 K hints towards the possibility of multigap superconductivity in $LuOs_3B_2$ because the normalized heat capacity jump at T_c of $\frac{\Delta C}{\gamma_n T_c} \approx 1$ magnitude is smaller than the value expected (1.43) for a single-gap BCS superconductor. Figure 6(c) shows C/T versus T^2 at various magnetic fields showing the suppression of the critical temperature on the application of a magnetic field. We will use this data to extract the upper critical field as a function of temperature.

We now calculate the Wilson ratio (R_W) to get some idea about the strength of the electronic correlations in $LuOs_3B_2$ [44]. The Wilson ratio is defined as the ratio of the density of states obtained from the magnetic measurements to the density of states obtained from the heat capacity measurements, i.e., $R_W = \frac{\pi^2 K_B^2}{3\mu_B^2}\frac{\chi_P}{\gamma}$, $R_W = 1$ for a free-electron Fermi gas. Substituting $\chi_P = 57.2(1) \times 10^{-5}$ cm^3/mol and $\gamma_n = 14.28(9)$ mJ/mol K^2 for $LuOs_3B_2$, we get $R_W \approx 3$ at $T = 0$ K. The enhanced value of the Wilson ratio indicates strong correlations in the material, similar values of R_W have earlier been reported for kagome metals $LaRu_3Si_2$ [24], $ThRu_3Si_2$ [28], and YRu_3Si_2 [45].

To further support the strength of the electronic correlation in $LuOs_3B_2$ as suggested by the Wilson ratio, we calculate the Kadowaki-Woods ratio (KWR) [46,47], which is defined as A/γ^2, where A is the coefficient of the quadratic term in the low-temperature resistivity that occurs due to electron-electron scattering and γ is the normal-state Sommerfeld coefficient in the heat capacity. Substituting $A = 9.7 \times 10^{-3}$ μΩ cm K^{-2} and $\gamma = 14.28$ mJ/mol K^2, we get the KWR ≈48 μΩ cm mol^2 K^2 J^{-2} which indicates significant electronic correlations in $LuOs_3B_2$.

We now estimate various superconducting parameters using the expressions mentioned in Refs. [43,48]. We first extract the variation of the lower and upper critical fields H_{c1} and H_{c2} as a function of the temperature T from various field-dependent measurements presented above. The critical field data so obtained are shown in Fig. 7(a). The upper critical field H_{c2} obtained from different measurements are in excellent agreement with each other. We observe an unusual quasilinear dependence in $H_{c2}(T)$ with the slope $\frac{dH_{c2}}{dT}|_{T_c} = -6055$ Oe/K . The clean limit Werthamer-Helfand-Hohenberg (WHH) formula [48] is used

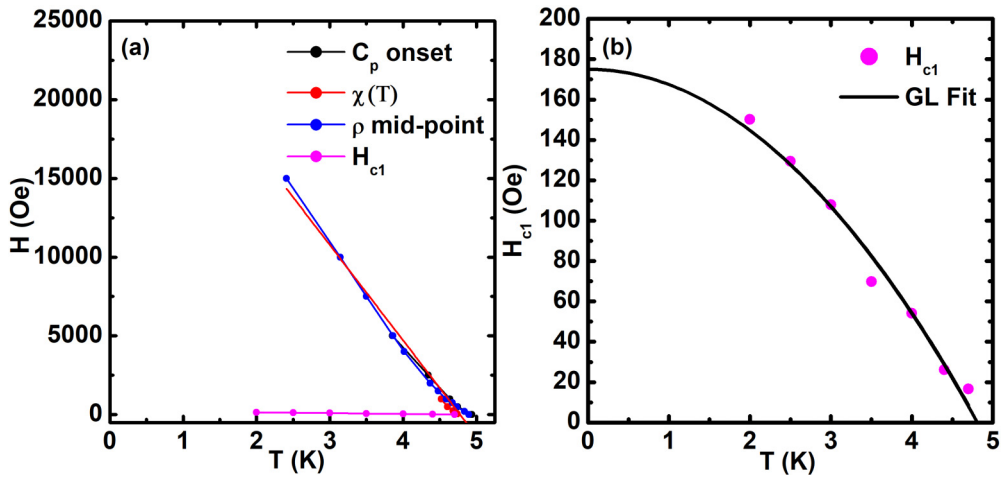

FIG. 7. (a) Variation of the lower critical field H_{c1} and the upper critical field H_{c2} as a function of temperature T from various measurements in finite magnetic field and (b) fitting of the lower critical field data to the Ginzburg-Landau equation.

TABLE I. Normal and superconducting state parameters for $LuOs_3B_2$. Here γ is the Sommerfeld coefficient, β is the coefficient of the T^3 term in the low-temperature heat capacity, θ_D is the Debye temperature, ξ is the superconducting coherence length, and λ is the penetration depth.

RRR	≈11
γ (mJ/mol K^2)	14.28
β (mJ/mol K^4)	0.261
θ_D (K)	355
$H_{c1}(0)$ (Oe)	175
$H_{c2}(0)$ (K Oe)	20.6
$H_c(0)$ (T)	1.2
T_C (K)	4.9
ξ_{GL} (nm)	12.57
λ_{GL} (nm)	153.2
κ_{GL}	12.2
λ_{ep}	0.54

to get an estimate of $H_{c2}(0) = -0.693 T_c \frac{dH_{c2}}{dT}|_{T_c} = 20.6$ K Oe . This value of $H_{c2}(0)$ is then used to estimate the coherence length ξ given by the expression $H_{c2} = \phi_0/2\pi\xi^2$, where $\phi_0 = hc/2e = 2.068 \times 10^{-7}$ G cm^2 is the flux quantum. We estimate $\xi = 12.57$ nm, using $H_{c2}(0) = 20.6$ KOe and $T_c \approx 4.9$ K. The lower critical field H_{c1} data are well fitted with the Ginzburg-Landau expressions: $H_{c1}(T) = H_{c1}(0)[1 - [\frac{T}{T_c}]^2]$ where $H_{c1}(0)$ is the lower critical field at 0 K and T_c is the transition temperature. The fitting shown in Fig. 7(b) gives the parameters $H_{c1}(0) = 175$ Oe and $T_c = 4.82$ K. The transition temperature obtained from the Ginzburg-Landau (GL) fit is in good agreement with bulk measurements presented previously. We can use the above values of ξ and $H_{c1}(0)$ to evaluate the penetration depth λ and Ginzburg-Landau parameter κ using the relation $\mu_0 H_{c1}(0) = \frac{\ln(\lambda/\xi)\Phi_0}{4\pi\lambda^2}$ and $\kappa = \lambda/\xi$, which gives $\lambda = 153.2$ nm and $\kappa = 12.2$. The large value of κ indicates that $LuOs_3B_2$ is a type-II superconductor. Using above values of $H_{c1}(0)$, $H_{c2}(0)$, and κ; we can also estimate the thermodynamic critical field $\mu_0 H_c(0)$ at 0 K by the expression: $H_{c1}(0) \times H_{c2}(0) = H_c^2(0)\ln(\kappa)$; which gives $H_c(0) = 1.2$ T. All superconducting parameters are collected in Table I.

An estimate of the electron-phonon coupling constant λ_{ep} can be made using McMillan's formula, which relates the superconducting transition temperature T_c to λ_{ep}, the Debye temperature θ_D, and the Coulomb coupling constant μ^* [49],

$$T_c = \frac{\theta_D}{1.45} \exp\left[-\frac{1.04(1+\lambda_{ep})}{\lambda_{ep} - \mu^*(1+0.62\lambda_{ep})}\right], \quad (1)$$

which can be inverted to give λ_{ep} in terms of T_c, θ_D, and μ^* as

$$\lambda_{ep} = \frac{1.04 + \mu^* \ln\left(\frac{\theta_D}{1.45T_c}\right)}{(1 - 0.62\mu^*)\ln\left(\frac{\theta_D}{1.45T_c}\right) - 1.04}. \quad (2)$$

We obtain $\lambda_{ep} = 0.54$ and 0.65 for $\mu^* = 0.10$ and 0.15, respectively, by using $\theta_D = 355$ K and using $T_c = 4.9$ K evaluated from the heat capacity measurements. These values of λ_{ep} suggest moderate electron-phonon coupling in $LuOs_3B_2$.

We discuss the properties of YCo_3B_2 now. The resistivity ρ versus temperature T for YCo_3B_2 measured between 2 and 300 K is shown in Fig. 8(a). The RRR ≈10 indicates a good quality sample. The $\rho(T)$ shows typical metallic behavior. The ρ data below ≈50 K can be fit by a Fermi-liquid behavior plus phonon contribution as $\rho(T) = \rho_0 + aT^2 + bT^5$. The fit is shown as the curve through the data in Fig. 8(a) inset. The fit gives the values $\rho_0 = 17.34(7)$ μΩ cm and $a = 2.2(6) \times 10^{-3}$ μΩ cm K^{-2}. The value of a, which is related to the strength of the electron-electron scattering, is enhanced and is similar to values found in heavy fermion materials. Below ∼10 K there is a weak upturn in the resistivity on lowering temperature. The resistivity upturn in metallic materials with magnetic ingredients (Co in this case) can occur due to the Kondo effect. However, we do not have sufficient data to conclude that. The heat capacity C for YCo_3B_2 below $T = 50$ K is shown in Fig. 8(b). The data below $T \sim 10$ K follows a Fermi-liquid behavior $C/T = \gamma + \beta T^2$. A fit to this expression is shown as the curve through the data in Fig. 8(b) inset and gave the value $\gamma = 12.83(4)$ mJ/mol K^2. The Kadowaki-Woods ratio $A/\gamma^2 \approx 13$ μΩ cm mol^2 K^2 J^{-2}, which is much larger than values found for transition metals close to magnetism like Ni, Pd but is close to the value observed for correlated metals like heavy fermion systems.

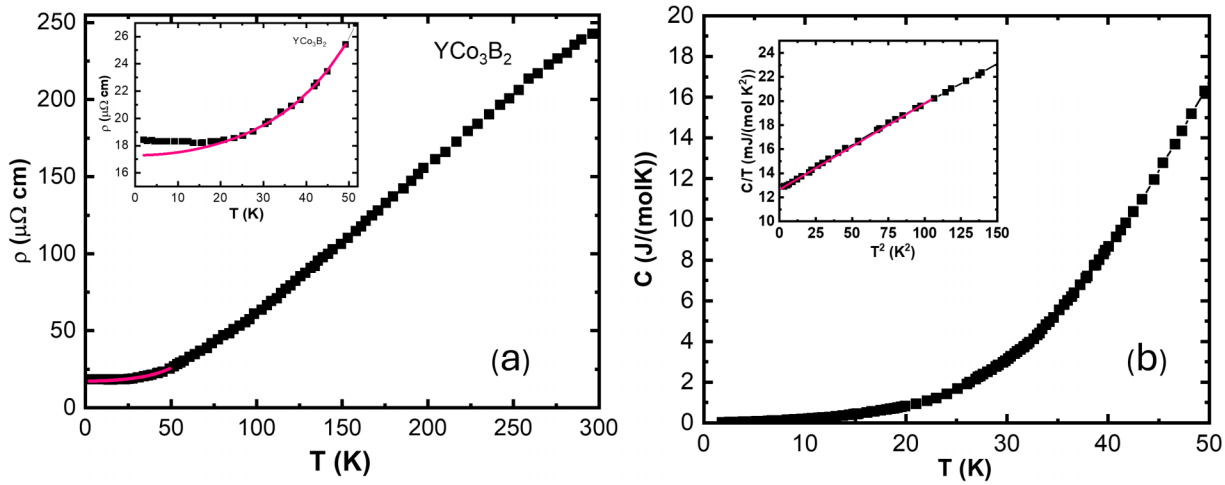

FIG. 8. (a) Resistivity and (b) heat capacity versus temperature at zero field for YCo_3B_2.

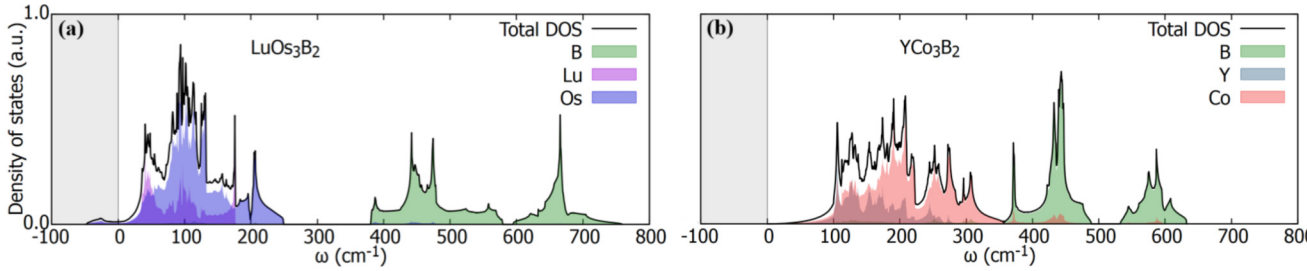

FIG. 9. (a) Phonon DOS for $LuOs_3B_2$ and (b) phonon DOS for YCo_3B_2.

C. Phonon calculations

The phonon density of states for $LuOs_3B_2$ and YCo_3B_2 are shown in Fig. 9. The contribution from different elements is displayed in different colors. The phonon DOS look quite different for the two materials. In YCo_3B_2 there are no imaginary modes, the *B* states have a gap around 500 cm^{-1}, and part of these *B* states overlap with the Co states. In the $LuOs_3B_2$ DOS we see imaginary modes. Also, the *B* states are well separated from the Os and Lu states. For both materials the low-frequency phonon modes mostly originate from Y or Lu atoms, while intermediate frequencies are essentially due to Co or Rh atoms; the manifold of low-dispersing bands for both materials is then due to the kagome network. Finally, the B atoms contribute to the high-frequency modes.

The phonon band structure is shown in Fig. 10. For $LuOs_3B_2$ we see that imaginary modes arise at high symmetry points Γ, *A*, and *L*. Imaginary modes in the phonon spectra point to an instability to structural distortions. While the imaginary modes at the Brillouin zone center may be attributed to a numerical approximation artifact, such as the finite size of the supercell, the mode at the *L* point drives the system toward a lower-energy configuration and a mildly distorted structure (Fig. 11). In particular, the DFT total energy of the distorted $2 \times 2 \times 2$ supercell is $E0 = -428.57006$ eV, while the total energy of $2 \times 2 \times 2$ pristine unit cells is $E0 = -428.11196$ eV.

The phonon bands for YCo_3B_2 are quite flat, similar to what is found for its electronic bands. From the phonon spectra, we compute the electron-phonon coupling λ_{e-ph}. The λ_{e-ph} for $LuOs_3B_2$ cannot be reliably determined due to the presence of imaginary phonon modes in the spectrum. In contrast, YCo_3B_2 does not exhibit such instabilities, and λ_{e-ph} can be evaluated in a standard manner, obtaining $\lambda_{e-ph} \approx 0.32$.

The Allen-Dynes formula can be used to estimate the superconducting critical temperature T_c [50,51]

$$T_c = \frac{\omega_{\log}}{1.2} \exp\left[\frac{-1.04(1+\lambda)}{\lambda(1-0.62\mu^*)-\mu^*}\right], \tag{3}$$

with $\omega_{\log}$ being related to the Eliashberg function

$$\omega_{\log} = \exp\left[\frac{2}{\lambda}\int \frac{d\omega}{\omega}\alpha^2 F(\omega)\ln\omega\right]. \tag{4}$$

Due to the presence of imaginary phonon modes in $LuOs_3B_2$, a quantitative estimate of the superconducting critical temperature from electron-phonon coupling is not reliable. Accordingly, we do not discuss calculated T_c values for this material, and instead rely on experimental measurements to characterize the superconducting transition. In contrast, YCo_3B_2 shows no such instabilities. Here the T_c is estimated to be close to 0 K, consistent with no superconductivity observed down to 2 K as can be seen from Fig. 10.

V. SUMMARY AND DISCUSSION

The family of kagome metals RT_3B_2 has a structure built up of kagome planes of *T* stacked along the *c*-axis with R-B planes separating the kagome planes. We studied RT_3B_2

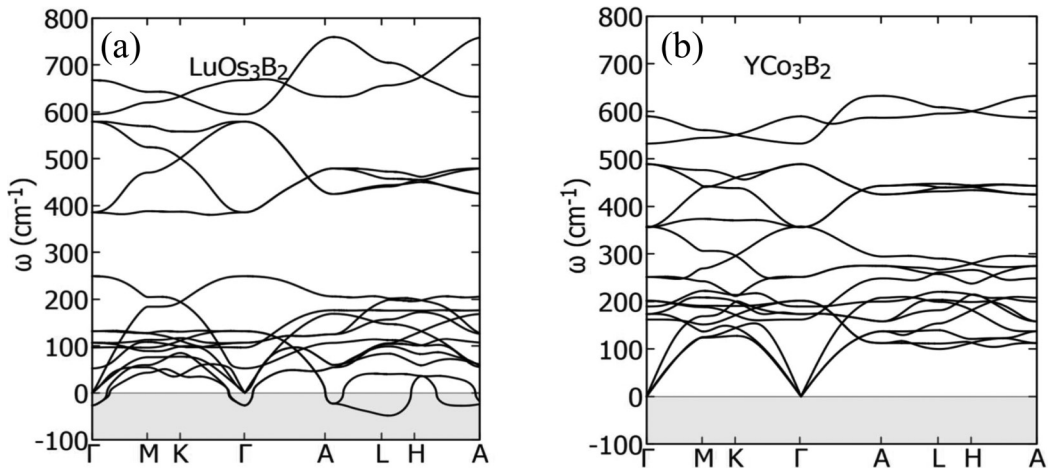

FIG. 10. Phonon dispersion along high-symmetry lines for (a) $LuOs_3B_2$ and (b) YCo_3B_2.

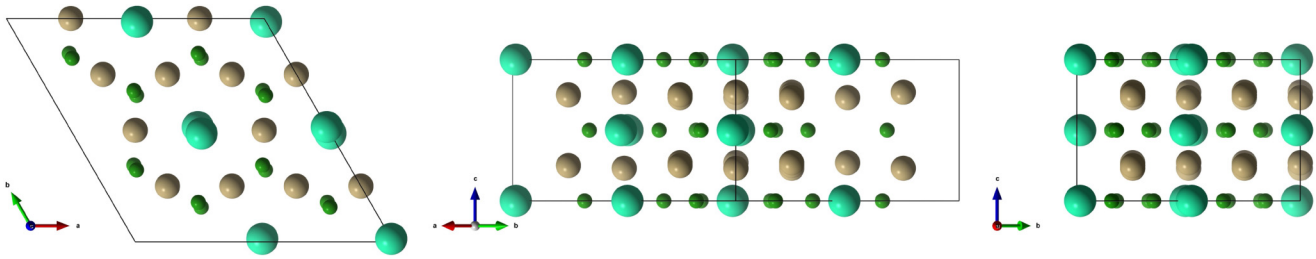

FIG. 11. The $2 \times 2 \times 2$ supercell of $LuOs_3B_2$, with atoms displaced according to the L phonon mode, seen from different perspectives. Lu atoms are colored with turquoise green, Os atoms with khaki, and B atoms with grass green.

(R = Y, Lu, and T = Co, Os) through measurements of their electrical transport, magnetic susceptibility, and heat capacity and through calculations of their electronic band structure, Fermi surfaces, and phonon spectrum. The electronic structure contains all the features expected for a 2D kagome lattice including a flat band, Dirac bands and van Hove singularities at high symmetry points in the Brillouin zone and the kagome planes made out of Co or Os make a dominant contribution to these features. The various measurements point to the importance of electron correlation as seen in the enhanced values of the Wilson ratio (∼3) and the Kadowaki-Woods ratio (∼48) for $LuOs_3B_2$ and the Kadowaki-Woods ratio (∼13) for YCo_3B_2.

The superconducting properties of $LuOs_3B_2$ with a T_c = 4.8 K points to type-II superconductivity with intermediate to strong electron-phonon coupling. The jump in the heat capacity at T_c is smaller than expectation for a single-gap s-wave BCS superconductor, suggesting that $LuOs_3B_2$ could be a multigap superconductor. Spectroscopic measurements of the gap could be useful to clarify this.

The phonon calculations for $LuOs_3B_2$ show imaginary modes, especially at the L high-symmetry point. Imaginary modes in the phonon spectra indicate an instability to structural distortions and may point to a susceptibility of the system to charge order or CDW-like states. Our measurements did not reveal any such transitions in the temperature range studied. However, it is possible that $LuOs_3B_2$ may be situated at a tipping point and small perturbations like doping or pressure could push the system towards such an instability. We recall that in $LaRh_3B_2$, which we reported on previously, showed no significant features of electronic correlations and no imaginary modes in its phonon spectra. The fact that we observe both strong correlations and imaginary phonon modes for $LuOs_3B_2$ points to an intimate connection between the two. Thus, $LuOs_3B_2$ seems to be a good candidate for further study through doping or pressure to try to explore the interplay between correlations and phonon anomalies.

On the other hand in YCo_3B_2, which has a large density of states just below E_F, it may also be interesting to dope the system to lower E_F into the large DOS. The small electron-phonon coupling calculated for YCo_3B_2 gives a likely reason for the absence of superconductivity in this material. Additionally, for YCo_3B_2 the band-structure and Fermi surface calculations show that this material is electrically anisotropic and is effectively insulating in the kagome plane and conducting along the c-axis. It may, therefore,, be of interest to synthesize mono-layer sheets of YCo_3B_2 which may be a candidate insulating kagome magnet.

Recently we became aware of a report on the synthesis, physical properties, and electronic band-structure calculations of $LuOs_3B_2$ [52]. Our superconducting and electronic structure properties are in qualitative agreement with those reported in Ref. [52]. However, we note that this paper reports the synthesis of single-phase samples of $LuOs_3B_2$ by arc-melting whereas we found $LuOs_3B_2$ to be incongruently melting and therefore not possible to obtain in single phase by arc-melting.

ACKNOWLEDGMENTS

We thank the X-ray, SEM, and liquid Helium central facilities at IISER Mohali. Y.S. acknowledges support from SERB Project No. CRG/2022/000015 and STARS project STARS-1/240, A.C. acknowledges support from PNRR MUR Project No. PE0000023-NQSTI. A.C., D.D.S., and R.T. acknowledge the Gauss Centre for Supercomputing e.V. [53] for funding this project by providing computing time on the GCS Supercomputer SuperMUC-NG at Leibniz Supercomputing Centre [54].

DATA AVAILABILITY

The data that support the findings of this article are not publicly available. The data are available from the authors upon reasonable request.

[1] L. Balents, Spin liquids in frustrated magnets, Nature (London) **464**, 199 (2010).

[2] L. Savary and L. Balents, Quantum spin liquids: A review, Rep. Prog. Phys. **80**, 016502 (2017).

[3] C. Broholm, R. J. Cava, S. A. Kivelson, D. G. Nocera, M. R. Norman, and T. Senthil, Quantum spin liquids, Science **367**, eaay0668 (2020).

[4] J. Knolle and R. Moessner, A field guide to spin liquids, Annu. Rev. Condens. Matter Phys. **10**, 451 (2019).

[5] M. Fu, T. Imai, T.-H. Han, and Y. S. Lee, Evidence for a gapped spin-liquid ground state in a kagome Heisenberg antiferromagnet, Science **350**, 655 (2015).

[6] T.-H. Han, J. S. Helton, S. Chu, D. G. Nocera, J. A. Rodriguez-Rivera, C. Broholm, and Y. S. Lee, Fractionalized excitations

in the spin-liquid state of a kagome-lattice antiferromagnet, Nature (London) **492**, 406 (2012).

[7] C. Balz, B. Lake, J. Reuther, H. Luetkens, R. Schönemann, T. Herrmannsdörfer, Y. Singh, A. T. M. N. Islam, E. M. Wheeler, J. Rodriguez-Rivera, T. Guidi, G. Simeoni, C. Baines, and H. Ryll, Physical realization of a quantum spin liquid based on a complex frustration mechanism, Nat. Phys. **12**, 942 (2016).

[8] Y. Okamoto, M. Nohara, H. Aruga-Katori, and H. Takagi, Spin-liquid state in the $s = 1/2$ hyperkagome antiferromagnet $Na_4Ir_3O_8$, Phys. Rev. Lett. **99**, 137207 (2007).

[9] Y. Singh, Y. Tokiwa, J. Dong, and P. Gegenwart, Spin liquid close to a quantum critical point in $Na_4Ir_3O_8$, Phys. Rev. B **88**, 220413(R) (2013).

[10] I. Mazin, H. Jeschke, F. Lechermann, H. Lee, M. Fink, R. Thomale, and R. Valentí, Theoretical prediction of a strongly correlated dirac metal, Nat. Commun. **5**, 4261 (2014).

[11] M. Kang, L. Ye, S. Fang, J. You, A. Levitan, M. Han, J. Facio, C. Jozwiak, A. Bostwick, E. Rotenberg, M. Chan, R. McDonald, D. Graf, K. Kaznatcheev, E. Vescovo, D. Bell, E. Kaxiras, J. van den Brink, M. Richter, M. P. Ghimire, *et al.*, Dirac fermions and flat bands in the ideal kagome metal FeSn, Nat. Mater. **19**, 163 (2020).

[12] M. Kang, S. Fang, L. Ye, H. Po, J. Denlinger, C. Jozwiak, A. Bostwick, E. Rotenberg, E. Kaxiras, J. Checkelsky, and R. Comin, Topological flat bands in frustrated kagome lattice CoSn, Nat. Commun. **11**, 4004 (2020).

[13] M. Li, Q. Wang, G. Wang, Z. Yuan, W. Song, R. Lou, Z. Liu, Y. Huang, Z. Liu, H. Lei, Z. Yin, and S. Wang, Dirac cone, flat band and saddle point in kagome magnet YMn_6Sn_6, Nat. Commun. **12**, 3129 (2021).

[14] B. R. Ortiz, L. C. Gomes, J. R. Morey, M. Winiarski, M. Bordelon, J. S. Mangum, I. W. H. Oswald, J. A. Rodriguez-Rivera, J. R. Neilson, S. D. Wilson, E. Ertekin, T. M. McQueen, and E. S. Toberer, New kagome prototype materials: Discovery of KV_3Sb_5, RbV_3Sb_5, and CsV_3Sb_5, Phys. Rev. Mater. **3**, 094407 (2019).

[15] B. R. Ortiz, S. M. L. Teicher, Y. Hu, J. L. Zuo, P. M. Sarte, E. C. Schueller, A. M. M. Abeykoon, M. J. Krogstad, S. Rosenkranz, R. Osborn, R. Seshadri, L. Balents, J. He, and S. D. Wilson, CsV_3Sb_5: A $\mathbb{Z}_2$ topological kagome metal with a superconducting ground state, Phys. Rev. Lett. **125**, 247002 (2020).

[16] B. R. Ortiz, P. M. Sarte, E. M. Kenney, M. J. Graf, S. M. L. Teicher, R. Seshadri, and S. D. Wilson, Superconductivity in the $\mathbb{Z}_2$ kagome metal KV_3Sb_5, Phys. Rev. Mater. **5**, 034801 (2021).

[17] S.-Y. Yang, Y. Wang, B. R. Ortiz, D. Liu, J. Gayles, E. Derunova, R. Gonzalez-Hernandez, L. Šmejkal, Y. Chen, S. S. P. Parkin, S. D. Wilson, E. S. Toberer, T. McQueen, and M. N. Ali, Giant, unconventional anomalous Hall effect in the metallic frustrated magnet candidate, KV_3Sb_5, Sci. Adv. **6**, eabb6003 (2020).

[18] H. Ku, G. Meisner, F. Acker, and D. Johnston, Superconducting and magnetic properties of new ternary borides with the $CeCo_3B_2$-type structure, Solid State Commun. **35**, 91 (1980).

[19] H. Barz, New ternary superconductors with silicon, Mater. Res. Bull. **15**, 1489 (1980).

[20] J. Vandenberg and H. Barz, The crystal structure of a new ternary silicide in the system rare-earth-ruthenium-silicon, Mater. Res. Bull. **15**, 1493 (1980).

[21] S. K. Malik, A. M. Umarji, G. K. Shenoy, A. T. Aldred, and D. G. Niarchos, Magnetism and superconductivity in the system $Ce_{1-x}La_xRh_3B_2$, Phys. Rev. B **32**, 4742 (1985).

[22] K. Athreya, L. Hausermann-Berg, R. Shelton, S. Malik, A. Umarji, and G. Shenoy, Superconductivity in the ternary borides $CeOs_3B_2$ and $CeRu_3B_2$: Magnetic susceptibility and specific heat measurements, Phys. Lett. A **113**, 330 (1985).

[23] U. Rauchschwalbe, W. Lieke, F. Steglich, C. Godart, L. C. Gupta, and R. D. Parks, Superconductivity in a mixed-valent system: $CeRu_3Si_2$, Phys. Rev. B **30**, 444 (1984).

[24] S. Li, B. Zeng, X. Wan, J. Tao, F. Han, H. Yang, Z. Wang, and H.-H. Wen, Anomalous properties in the normal and superconducting states of $LaRu_3Si_2$, Phys. Rev. B **84**, 214527 (2011).

[25] S. Li, J. Tao, X. Wan, X. Ding, H. Yang, and H.-H. Wen, Distinct behaviors of suppression to superconductivity in $LaRu_3Si_2$ induced by Fe and Co dopants, Phys. Rev. B **86**, 024513 (2012).

[26] B. Li, S. Li, and H.-H. Wen, Chemical doping effect in the $LaRu_3Si_2$ superconductor with a kagome lattice, Phys. Rev. B **94**, 094523 (2016).

[27] C. Mielke, Y. Qin, J.-X. Yin, H. Nakamura, D. Das, K. Guo, R. Khasanov, J. Chang, Z. Q. Wang, S. Jia, S. Nakatsuji, A. Amato, H. Luetkens, G. Xu, M. Z. Hasan, and Z. Guguchia, Nodeless kagome superconductivity in $LaRu_3Si_2$, Phys. Rev. Mater. **5**, 034803 (2021).

[28] Y. Liu, J. Li, W.-Z. Yang, J.-Y. Lu, B.-Y. Cao, H.-X. Li, W.-L. Chai, S.-Q. Wu, B.-Z. Li, Y.-L. Sun, W.-H. Jiao, C. Wang, X.-F. Xu, Z. Ren, and G.-H. Cao, Superconductivity in kagome metal $ThRu_3Si_2$, Chin. Phys. B **33**, 057401 (2024).

[29] S. Chaudhary, Shama, J. Singh, A. Consiglio, D. Di Sante, R. Thomale, and Y. Singh, Role of electronic correlations in the kagome-lattice superconductor $LaRh_3B_2$, Phys. Rev. B **107**, 085103 (2023).

[30] G. Kresse and J. Hafner, *Ab initio* molecular dynamics for liquid metals, Phys. Rev. B **47**, 558 (1993).

[31] G. Kresse and J. Hafner, *Ab initio* molecular-dynamics simulation of the liquid-metal–amorphous-semiconductor transition in germanium, Phys. Rev. B **49**, 14251 (1994).

[32] G. Kresse and J. Furthmüller, Efficient iterative schemes for ab initio total-energy calculations using a plane-wave basis set, Phys. Rev. B **54**, 11169 (1996).

[33] G. Kresse and J. Furthmüller, Efficiency of *ab initio* total energy calculations for metals and semiconductors using a plane-wave basis set, Comput. Mater. Sci. **6**, 15 (1996).

[34] P. Giannozzi, O. Baseggio, P. Bonfà, D. Brunato, R. Car, I. Carnimeo, C. Cavazzoni, S. de Gironcoli, P. Delugas, F. Ferrari Ruffino, A. Ferretti, N. Marzari, I. Timrov, A. Urru, and S. Baroni, QUANTUM ESPRESSO toward the exascale, J. Chem. Phys. **152**, 154105 (2020).

[35] P. Giannozzi, S. Baroni, N. Bonini, M. Calandra, R. Car, C. Cavazzoni, D. Ceresoli, G. L. Chiarotti, M. Cococcioni, I. Dabo, A. Dal Corso, S. de Gironcoli, S. Fabris, G. Fratesi, R. Gebauer, U. Gerstmann, C. Gougoussis, A. Kokalj, M. Lazzeri, L. Martin-Samos, *et al.*, QUANTUM ESPRESSO: A modular and open-source software project for quantum simulations of materials, J. Phys.: Condens. Matter **21**, 395502 (2009).

[36] P. Giannozzi, O. Andreussi, T. Brumme, O. Bunau, M. Buongiorno Nardelli, M. Calandra, R. Car, C. Cavazzoni, D. Ceresoli, M. Cococcioni, N. Colonna, I. Carnimeo, A. Dal Corso, S. de Gironcoli, P. Delugas, R. A. DiStasio, Jr.,

A. Ferretti, A. Floris, G. Fratesi, G. Fugallo, *et al.*, Advanced capabilities for materials modeling with QUANTUM ESPRESSO, J. Phys.: Condens. Matter **29**, 465901 (2017).

[37] G. Kresse and D. Joubert, From ultrasoft pseudopotentials to the projector augmented-wave method, Phys. Rev. B **59**, 1758 (1999).

[38] J. P. Perdew, K. Burke, and M. Ernzerhof, Generalized gradient approximation made simple, Phys. Rev. Lett. **77**, 3865 (1996).

[39] D. R. Hamann, Optimized norm-conserving Vanderbilt pseudopotentials, Phys. Rev. B **88**, 085117 (2013).

[40] M. Wierzbowska, S. de Gironcoli, and P. Giannozzi, Origins of low- and high-pressure discontinuities of T_c in niobium, arXiv:cond-mat/050407.

[41] C. Chacon and O. Isnard, The structural and magnetic properties of $Y_{n+1}Co_{3n+5}B_{2n}$ compounds investigated by neutron diffraction, J. Phys.: Condens. Matter **13**, 5841 (2001).

[42] L. B. Mendelsohn, F. Biggs, and J. B. Mann, Hartree-Fock diamagnetic susceptibilities, Phys. Rev. A **2**, 1130 (1970).

[43] Y. Singh, A. Niazi, M. D. Vannette, R. Prozorov, and D. C. Johnston, Superconducting and normal-state properties of the layered boride OsB_2, Phys. Rev. B **76**, 214510 (2007).

[44] K. G. Wilson, The renormalization group: Critical phenomena and the kondo problem, Rev. Mod. Phys. **47**, 773 (1975).

[45] C. Gong, S. Tian, Z. Tu, Q. Yin, Y. Fu, R. Luo, and H. Lei, Superconductivity in kagome metal YRu_3Si_2 with strong electron correlations, Chin. Phys. Lett. **39**, 087401 (2022).

[46] M. J. Rice, Electron-electron scattering in transition metals, Phys. Rev. Lett. **20**, 1439 (1968).

[47] K. Kadowaki and S. Woods, Universal relationship of the resistivity and specific heat in heavy-fermion compounds, Solid State Commun. **58**, 507 (1986).

[48] Y. Singh, C. Martin, S. L. Bud'ko, A. Ellern, R. Prozorov, and D. C. Johnston, Multigap superconductivity and Shubnikov–de Haas oscillations in single crystals of the layered boride OsB_2, Phys. Rev. B **82**, 144532 (2010).

[49] W. L. McMillan, Transition temperature of strong-coupled superconductors, Phys. Rev. **167**, 331 (1968).

[50] R. Dynes and P. Allen, Transition temperature of strong-coupled superconductors reanalyzed, Phys. Rev. B **12**, 1720 (1975).

[51] J. P. Carbotte, Properties of boson-exchange superconductors, Rev. Mod. Phys. **62**, 1027 (1990).

[52] Y. Xiao, Q. Duan, T. jia, Y. Cui, S. Liu, Z. Wen, L. Ji, R. Zhong, Y. Chen, and Y. Zhao, Superconductivity and electron correlations in the kagome metal $LuOs_3B_2$, Phys. Rev. B **111**, 195132 (2025).

[53] https://www.gauss-centre.eu.

[54] https://www.lrz.de.